Probing the timescale of the exchange interaction in a ferromagnetic alloy

Stefan Mathias[a,b,1,2], Chan La-O-Vorakiat[a,1], Patrik Grychtol[a,c], Patrick Granitzka[a,b], Emrah Turgut[a], Justin M. Shaw[d], Roman Adam[c], Hans T. Nembach[d], Mark E. Siemens[a,e], Steffen Eich[b], Claus M. Schneider[c], Thomas J. Silva[d], Martin Aeschlimann[b], Margaret M. Murnane[a], and Henry C. Kapteyn[a]

[a]Department of Physics and JILA, University of Colorado, Boulder, CO 80309-0440; [b]University of Kaiserslautern and Research Center OPTIMAS, 67663, Kaiserslautern, Germany; [c]Peter Grünberg Institute, PGI-6, Research Center Jülich, 52425, Jülich, Germany; [d]Electromagnetics Division, National Institute of Standards and Technology, Boulder, CO 80305-3328; and [e]Department of Physics and Astronomy, University of Denver, Denver, CO 80208-6900

The underlying physics of all ferromagnetic behavior is the cooperative interaction between individual atomic magnetic moments that results in a macroscopic magnetization. In this work, we use extreme ultraviolet pulses from high-harmonic generation as an element-specific probe of ultrafast, optically driven, demagnetization in a ferromagnetic Fe-Ni alloy (permalloy). We show that for times shorter than the characteristic timescale for exchange coupling, the magnetization of Fe quenches more strongly than that of Ni. Then as the Fe moments start to randomize, the strong ferromagnetic exchange interaction induces further demagnetization in Ni, with a characteristic delay determined by the strength of the exchange interaction. We can further enhance this delay by lowering the exchange energy by diluting the permalloy with Cu. This measurement probes how the fundamental quantum mechanical exchange coupling between Fe and Ni in magnetic materials influences magnetic switching dynamics in ferromagnetic materials relevant to next-generation data storage technologies.

magnetism | quantum | ultrafast

Progress in magnetic information storage and processing technology is intimately associated with complex materials that are engineered at the nanometer scale. Heat-assisted magnetic recording (1), bit-patterned data storage media (2), all-optical magnetization reversal (3), and giant tunneling magnetoresistive disk drive read sensors are examples of such technologies (4). Next-generation devices will require that the magnetic state of materials be manipulated on fast timescales and at the nanometer level. However, a complete microscopic understanding of magnetization dynamics that involves the correlated interactions of spins, electrons, photons, and phonons on femtosecond timescales has yet to be developed. Two reasons for this lack of fundamental understanding of ultrafast magnetism at the microscopic scale are the complexity of the problem itself, as well as the experimental challenge of accessing ultrafast and element-specific magnetization dynamics. One approach for addressing the experimental challenge is to use X-ray magnetic circular dichroism (XMCD) employing X-rays generated by a synchrotron light source. XMCD has the inherent advantage of element-specific detection, and "sliced" synchrotron pulses are already used for ultrafast studies (5–9). In an alternative approach, we recently demonstrated that coherent extreme ultraviolet (XUV) beams from a tabletop high-harmonic source (10, 11) can also be used to probe ultrafast element-specific magnetization dynamics in permalloy ($Ni_{0.8}Fe_{0.2}$) (12). For that demonstration, we took advantage of magnetic birefringence at the M-edge in transition metals to independently follow dynamics for Ni and Fe. However, the time resolution available in that initial experiment was insufficient to observe any differences in the response of the constituent elements on very short timescales.

In this work, we experimentally answer the fundamental question of whether the magnetization dynamics of individual elements in a ferromagnetic alloy can differ on ultrafast time-

scales. This is a very important fundamental question that has not been addressed either theoretically or experimentally to date, the answer to which reveals how the exchange interaction can control the ultrafast dynamics of elemental spin subsystems in complex materials. To answer this question, we rapidly excite permalloy with an ultrashort ($\approx$25 fs) laser pulse and probe the element-specific demagnetization dynamics using $<$10 fs high-harmonic pulses. The superior time resolution of our experiment allows us to observe that the magnetization dynamics of Fe and Ni are transiently delayed with respect to each other—by about 18 fs in permalloy and 76 fs in Cu-diluted permalloy $((Ni_{0.8}Fe_{0.2})_{1-x}Cu_x)$. We ascribe this transient decoupling in the magnetic behavior to the finite strength of the fundamental quantum exchange interaction between Fe and Ni atoms in the material. Specifically, for times shorter than the characteristic timescale for exchange coupling, the magnetization of Fe quenches more strongly than that of Ni. Then, as the Fe moments start to randomize, the strong ferromagnetic interatomic exchange interaction between Fe and Ni induces further demagnetization in Ni, with a characteristic delay determined by the strength of the Fe-Ni exchange interaction. Interatomic exchange energies of transition metal alloys are in the 10–100 meV range, yielding characteristic exchange times in the femtosecond range which corresponds to finite spin-flip scattering times of 10–100 fs (9). Our findings provide crucial information for open questions in femtosecond magnetization dynamics in the case of metallic, multispecies, exchange-coupled systems.

Results

In our experiment, sub-10 fs XUV light pulses from high-harmonic generation (HHG) are produced by focusing 2 mJ femtosecond laser pulses into a Ne-filled waveguide. The harmonic photon energy range of 35 to 72 eV spans the M absorption edges of Fe and Ni at $\approx$54 eV and $\approx$67 eV, respectively (see Fig. 2B). In the transverse magneto-optical Kerr-effect (T-MOKE) geometry used for these measurements, the intensity of the reflected HHG light is proportional to the magnetization transverse to the plane of incidence (12). We probe the magnetization by reflecting the XUV beam from a magnetic diffraction grating structure, as shown in Fig. 1A. We used gratings with 1 μm lines and a 2 μm period patterned in three different ways: (i) alternating
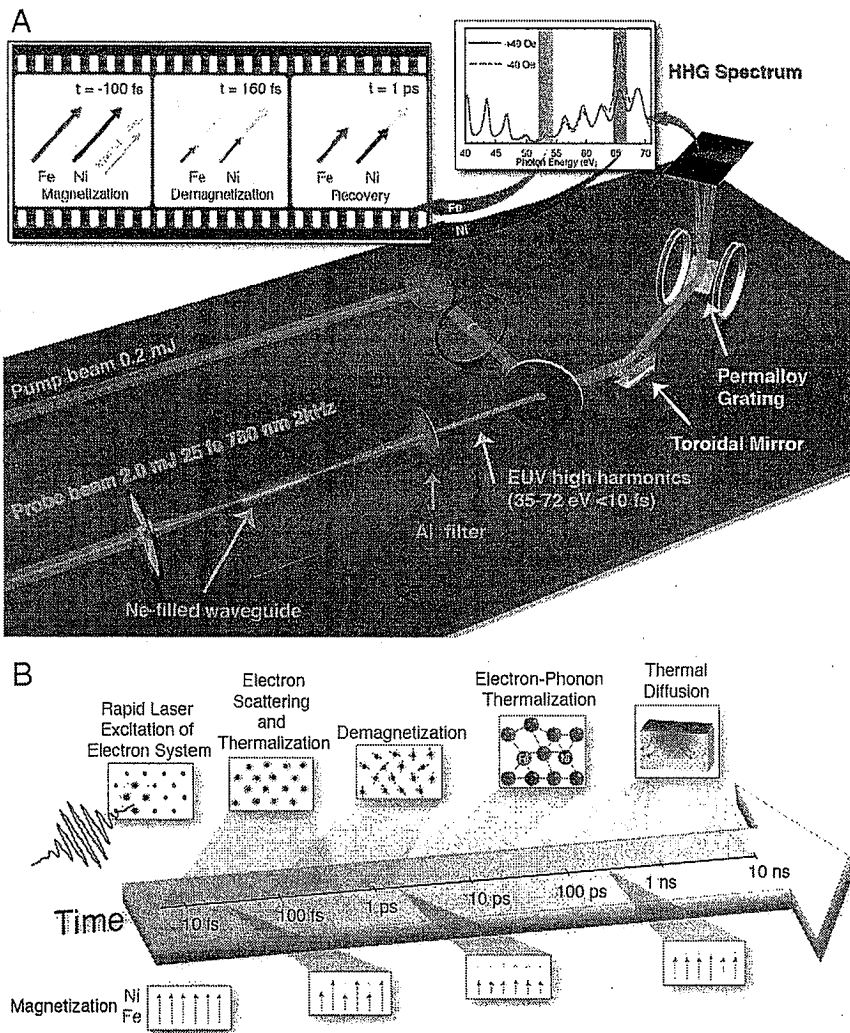
A

Fig. 1. Schematic of the physics and experiment. (*Top*) Ultrafast XUV pulses (*A*) are reflected from a permalloy grating sample, which spatially separates the harmonics to form a spectrum on a CCD camera. The reflected HHG intensity at the Fe and Ni M-shell absorption edges (red and blue) depends on the magnetization transverse to the optical plane of incidence that is periodically reversed by transverse-mounted Helmholtz coils. Exciting the sample with an infrared laser pulse (red) causes the material to demagnetize on femtosecond timescales. (*B*) After rapid excitation of the electron system by a femtosecond laser pulse, various scattering processes between electrons and phonons (with and without spin-flips) determine the dynamical response of the system. First, the strongly excited electron gas thermalizes by predominantly electron-electron scattering to a Fermi-Dirac distribution. The ferromagnet starts to demagnetize because of spin-flip scattering events during this thermalization process. Electron-phonon scattering processes transfer energy from the excited electron gas to the lattice, and thermal equilibrium is typically reached on picosecond timescales. Finally, on nanosecond timescales, the material cools by thermal diffusion. The red and blue arrows in the lower boxes show the observed distinct demagnetization dynamics of Fe and Ni in permalloy.

elemental Fe and Ni stripes to probe the behavior of the pure materials; (*ii*) permalloy ($Ni_{0.8}Fe_{0.2}$); and (*iii*) permalloy-Cu (($Ni_{0.8}Fe_{0.2})_{0.6}Cu_{0.4}$). The Curie temperature T_c for permalloy is 850 K, while for permalloy-Cu, $T_c \approx 400$ K. The HHG spectrum diffracted from the grating sample is focused onto an X-ray CCD camera. In order to determine the T-MOKE asymmetry, the change in reflected HHG intensity at the M-absorption edges is monitored while the magnetization direction of the sample is switched. The T-MOKE asymmetry parameter A is calculated from the experimental data as

$$A = \frac{I_+ - I_-}{I_+ + I_-},$$

where I_+ and I_- denote the reflected XUV intensities for the two magnetization directions. More details of the measurement method can be found in Refs. (12–14).

The asymmetry for the permalloy sample was measured using XUV radiation from both the HHG source and a synchrotron source. Fig. 2*A* shows the dependence of the magnetic asymmetry on the angle of incidence and photon energy in the form of a color-coded contour plot. Fe and Ni are easily distinguished by strong, element-specific T-MOKE asymmetry peaks that correspond to excitation of the localized M-shell electrons into unoccupied states above the Fermi energy. XUV T-MOKE is therefore similar to XMCD, providing a localized probe of magnetic moments. Moreover, the magnetic dynamics in pure Ni measured by XUV T-MOKE are in excellent agreement with visible MOKE probes

(14, 15). Note that both peaks for the two elements have widths of several eV. The magnetic asymmetry signal shows bipolar contributions over an extended energy range for Fe and Ni, below and above an energy of about 60 eV (white line in Fig. 2*A*), respectively (13). The detailed peak structure is made complicated by the convolution of the finite lifetime of the p-orbital holes and the weak splitting of the shallow M_2 and M_3 levels. The splitting is largest for Ni.

The largest magnetic asymmetry occurs at an angle of incidence of 45° (black dashed line in Fig. 2*A*, which corresponds to the geometry used in the HHG setup). Fig. 2*B* shows the measured magnetic asymmetries using synchrotron and HHG light at a 45° angle of incidence. The spectra are in good agreement with each other. We attribute the minor discrepancies to the qualitatively different spectra for HHG and synchrotron radiation, which is composed of discrete harmonic lines for HHG and is a quasicontinuum for synchrotron radiation. The good agreement in the asymmetry spectra between the HHG and synchrotron sources validates our approach for measuring ultrafast demagnetization dynamics using HHG radiation.

For these measurements, the sample is transiently demagnetized using a focused ultrafast laser pump pulse (25 fs duration, 780 nm wavelength) that rapidly excites the electronic system. After the excitation of the electron system in the material, various scattering processes between electrons and phonons (with and without spin-flips) determine the dynamical response of the system on femtosecond to nanosecond timescales (see Fig. 1*B*). In our experiment, the demagnetization is captured by measuring
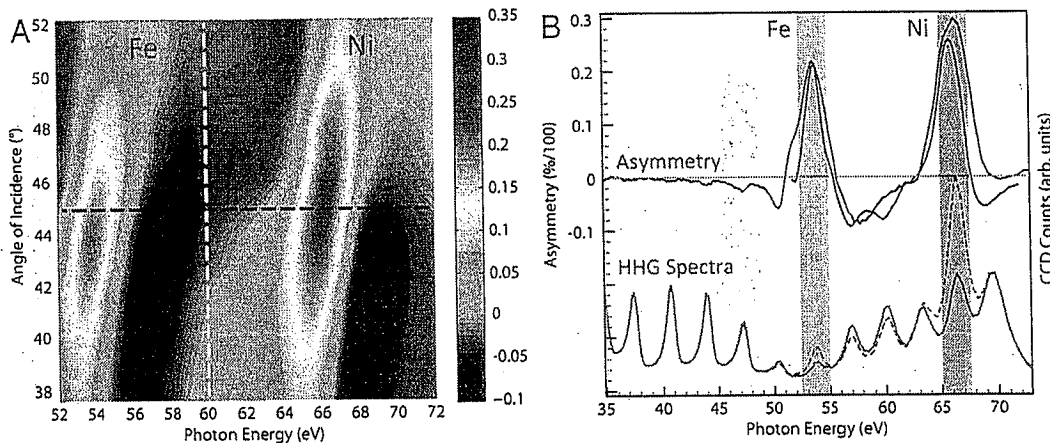
Fig. 2. XUV spectra and magnetic asymmetry. (A) Magnitude of the asymmetry, coded in color, as a function of photon energy and angle of incidence, measured using synchrotron radiation. The asymmetry signal of Fe (≈ 54 eV) is clearly separated from Ni (≈ 67 eV). (B) HHG XUV spectra reflected from the permalloy grating sample at an angle of incidence of 45°, shown as green solid and dotted lines for the two different magnetization directions. The blue line is the calculated asymmetry from the HHG spectra, and the black line the asymmetry from synchrotron data that corresponds to the spectral cut shown as a black dashed line in (A).

the asymmetry A as a function of time delay between the infrared pump and the XUV probe pulses (see Movie S1). We start with a simultaneous measurement of the demagnetization dynamics of elemental Fe and Ni using a sample with interleaved stripes of Fe and Ni (Fig. 3A). After excitation at a laser fluence of ≈ 2 mJ/cm^2, the magnetization decreases rapidly and is quenched by about 19% for Fe and 45% for Ni. Using a double exponential fitting function (16) given by $m(t) = 1 - \Delta m[1 - \exp(-t/\tau_m)]\exp(-t/\tau_r)$, we measure demagnetization times of $\tau_m = 98 \pm 26$ fs for Fe and 157 ± 9 fs for Ni (with recovery time constants $\tau_r = 11 \pm 7$ ps for Fe, and $\tau_r = 9 \pm 1$ ps for Ni, respectively), in agreement with earlier studies (17, 18).

Now, moving from single-species metals to the more complex binary alloy permalloy, where the constituents Fe and Ni are miscible and strongly exchange coupled—one might expect identical demagnetization dynamics for the two elements if one assumes a completely delocalized, itinerant spin-polarized band structure i.e. if the Fe and Ni contributions to the magnetization are indistinguishable. If this were the case, even though T-MOKE probes the local magnetic signal in the vicinity of the Fe and Ni atoms, one would expect identical demagnetization timescales at the two different sites. Note here the inherent difference between our measurements in a strongly coupled 3d ferromagnetic system and a recent study by Radu et al. of demagnetization dynamics in the 3d-4f ferrimagnet GdFeCo (9). In that work, distinctly different dynamics of the weakly exchange-coupled elements arranged in sublattices were observed, a natural consequence of the different temperature-dependent properties of the localized 4f Gd moment and less localized 3d Fe moment when in thermodynamic equilibrium (a property that gives rise to a magnetic compensation point whereby the rare earth and transition metal sublattices are of equal but opposite magnetic moment).

Fig. 3B shows the measured element-specific demagnetization of Fe and Ni in permalloy following excitation by a pump pulse with fluence of ≈ 2 mJ/cm^2. As expected in a strongly exchange coupled 3d alloy, the magnetization decreases rapidly for both elements to a common minimum of about 70% of the total magnetization. Somewhat surprisingly, however, an inspection of the data on short timescales clearly shows that the demagnetization of Fe precedes that of Ni by approximately 10–20 fs (*Inset*, Fig. 3B). This relative difference between Fe and Ni in permalloy was not previously observed in Ref. (12), because the temporal resolution in that experiment was insufficient to resolve such a small shift in the onset of demagnetization. We stress that the demagnetization data for Fe and Ni are collected *at the same time* in this measurement, precluding any mismatch between the two

elements in the determination of the arrival time for the pump and probe pulses.

The experimental results of Fig. 3B directly demonstrate that the spin-dependent part of the electronic wave functions in the itinerant 3d bands must also exhibit a local character. Differing dynamics in the vicinity of the Fe and Ni atoms shows that contributions of Fe and Ni to the total magnetic moment can be clearly distinguished. This is a very surprising result, and since we focus in the following discussion on the origin of these distinguishable parts of the Fe and Ni magnetic contributions, we for simplicity denote them as demagnetization dynamics of Fe and Ni, respectively.

The degree to which demagnetization dynamics can be different for Fe and Ni in permalloy necessarily depends on the strength of the Fe-Ni interatomic exchange coupling between neighboring magnetic moments: the weaker the Fe-Ni exchange coupling, the more the dynamics can differ without incurring too large of an energy cost. In the particular case of permalloy, the interatomic exchange coupling is substantial, as indicated by the Curie temperature T_C of 850 K. Motivated by this line of reasoning, we repeated our measurements with the tertiary alloys of permalloy diluted by Cu (permalloy-Cu). Fe, Ni, and Cu are all miscible at room temperature when one dilutes permalloy with Cu (19, 20). The alloying of Cu with permalloy results in a continuous reduction of the volume-averaged exchange parameter through the reduction of the number of ferromagnetic nearest-neighbor atoms. Such alloys also retain the high permeability associated with pure permalloy and avoid any discontinuous crystallographic phase transitions with varying Cu content. This, in turn, provides us with the ability to tune T_C (see *Supporting Information*) over a broad temperature range. For fixed temperature measurements, the exchange coupling is further reduced by the concomitant renormalization of the effective exchange integral near T_C (21, 22).

We prepared a sample of $(Ni_{0.8}Fe_{0.2})_{0.6}Cu_{0.4}$ by cosputtering from permalloy and Cu targets. X-ray diffraction verified that our samples are a solid solution (i.e., random placement of the Fe, Ni, and Cu atoms in the crystal lattice) fcc phase (see *Methods and Materials* and *Supporting Information*). Fig. 3C shows a plot of the element-selective, time-resolved T-MOKE signal for a permalloy-Cu sample with $T_C = 406 \pm 3$ K. We unambiguously observe a significant demagnetization delay for Ni of approximately 76 fs relative to Fe, as indicated by the arrows. Interestingly, after accounting for the delay in the demagnetization, the exponential decay of the magnetization for each of the elements is *identical* within our error bars, yielding fitted values for the effective demagnetization time τ_{Eff} of 242 ± 12 fs for Fe and
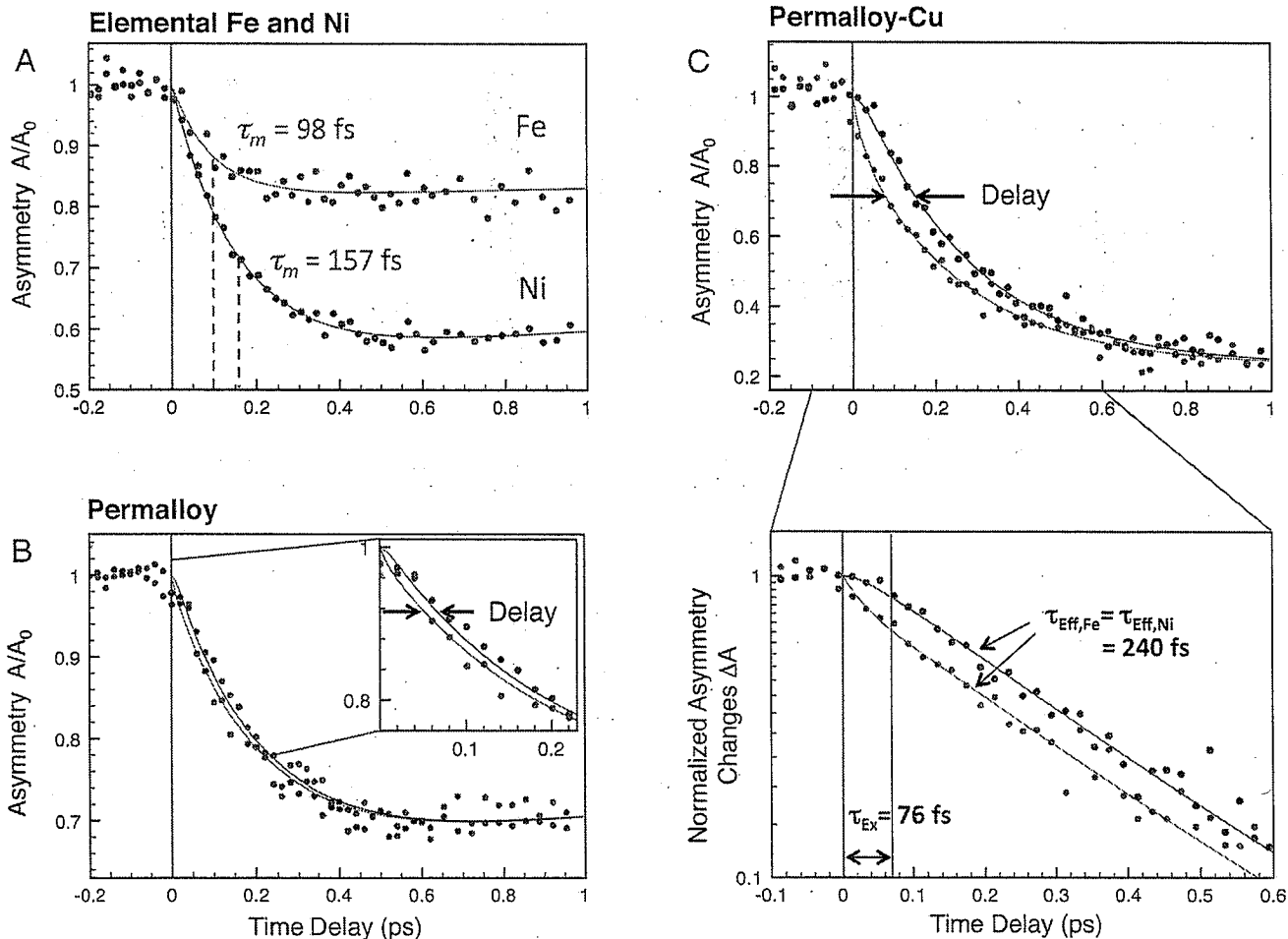
Fig. 3. Ultrafast demagnetization of Fe (red dots) and Ni (blue dots) for elemental Fe and Ni (*A*), in permalloy (*B*), and in permalloy-Cu (*C*). Simple exponential decay fits yield the demagnetization constants of (*A*) elemental Fe and Ni, and "effective" demagnetization constants τ_{Eff} for Fe and Ni in (*B*) permalloy, and (*C*) permalloy-Cu, data set (see text). Fits to the model (solid lines) are used to extract the intrinsic demagnetization times for Fe and Ni in the alloys, τ_{Fe} and τ_{Ni}, as well as the exchange time τ_{Ex}, after which the Fe and Ni spin baths return to equilibrium with respect to each other with an effective demagnetization time constant of τ_{Eff}. The data for permalloy-Cu (*C*) is also shown in log-scale as a function of the normalized asymmetry changes $\Delta A = (A-A_{min})/(A_0-A_{min})$, where A_0 the total asymmetry and A_{min} the minimum asymmetry reached in the demagnetization process. We stress that the demagnetization data for Fe and Ni are collected *at the same time* in this measurement, precluding any mismatch between the two elements in the determination of time-zero between pump and probe laser pulses.

236 ± 13 fs for Ni. (Note the difference between the effective demagnetization time of the respective element in the alloy and the intrinsic elemental demagnetization times used in the model presented below).

Discussion

The dynamics of ultrafast demagnetization are complex. A proven theory that completely describes all the interactions between photons, electrons, spins, and phonons at a microscopic level does not yet exist. However, it is known that femtosecond infrared pulses coherently interact with the electric charges and spins in the material within ≈ 0–50 fs (23). Subsequently, the highly excited electrons relax to a thermalized population, accompanied by spin-flip scattering processes that lead to ultrafast demagnetization on timescales of ≈ 100–$1,000$ fs (Fig. 1*B*) (18, 24–27). These details of the scattering processes remain the subject of intense debate in ultrafast magnetism (7, 24, 25, 28–33). Moreover, nonadiabatic heating processes of the electron, spin, and lattice subsystems on such ultrafast timescales, together with strongly nonequilibrium transient phase states, necessarily complicate our understanding of the underlying physics for ultrafast demagnetization. It is therefore important to include the laser-induced hot electrons in a discussion of magnetic dynamics on such ultrashort <100 fs timescales.

Hot electrons can induce demagnetization by superdiffusive spin transport (33), and also by screening the Coulomb potentials on femtosecond timescales (34, 35). While superdiffusive spin transport leads to a direct demagnetization process, screening might indirectly act on the magnetization of the material by transiently modifying the exchange interaction in ferromagnetic conductors (36) during the 100–500 fs needed for the relaxation of the pump-induced highly excited electrons. Such a modification of the exchange interaction then has been shown to directly influence the ultrafast magnetization dynamics (37). Note that the screening process itself evolves on attosecond timescales in metals, but is active until the highly excited electrons relax their energy. If superdiffusive spin transport or any hot-electron induced modification of the exchange coupling contributed significantly to the observed delay of the demagnetization dynamics of Fe and Ni in permalloy, then we would expect a strong dependence of the delay times on the pump fluence, since the pump fluence controls the number of excited hot electrons. However, the demagnetization delays for permalloy-Cu do not change when the pump fluence is varied between 250 and 360 mW, which corresponds to a variation in the relative change in magnetization, $\Delta M/M$, between about 50% and 80%, respectively (data shown in *Supporting Information*). We therefore conclude that neither superdiffusive spin transport nor a transient modification of

the exchange interaction (e.g. due to hot electrons) are the dominant processes causing the demagnetization delay of Ni. Rather, the demagnetization delay between Ni and Fe in permalloy and permalloy-Cu is an intrinsic property that depends upon the strength of the interatomic Fe–Ni exchange interaction, since the demagnetization delay is increased when the exchange interaction is reduced in permalloy-Cu.

To gain more physical insight into demagnetization dynamics in ferromagnetic systems, we need to take the interatomic Fe–Ni exchange coupling into account. Our data clearly shows that using a double exponential fitting function for elemental Fe and Ni is not sufficient to describe the coupled dynamics in the alloyed systems. Therefore, to extract quantitative timescales for the demagnetization process, we modeled our experimental data using the following first-order coupled rate equations:

$$\frac{dm_{Fe}}{dt} = -\frac{m_{Fe}}{\tau_{Fe}} - \frac{m_{Fe} - m_{Ni}}{\tau_{Ex}} \qquad [1a]$$

$$\frac{dm_{Ni}}{dt} = -\frac{m_{Ni}}{\tau_{Ni}} - \frac{m_{Ni} - m_{Fe}}{\tau_{Ex}} \qquad [1b]$$

where m_{Fe} and m_{Ni} are the normalized Fe and Ni magnetizations, τ_{Fe} and τ_{Ni} are the intrinsic decay times for Fe and Ni in the absence of exchange coupling between them, and τ_{Ex} the characteristic "exchange time" that describes the thermodynamic coupling of spins in the Fe and Ni systems. Solving the equations for the limit where $\tau_{Fe} \ll \tau_{Ni}$, τ_{Ex} emerges as the delay time between Fe and Ni, where both species have the same effective time constant τ_{Eff} (See Fig. 3B); i.e., the exchange time and the measured delay time are equivalent quantities. The solution for the initial condition $m_{Fe}(t = 0) = m_{Ni}(t = 0) = 1$ is:

$$m_{Fe}(t) = \left[\frac{1 - \eta_-}{\eta_+ - \eta_-}\right] e^{-\lambda_+ t} - \left[\frac{1 - \eta_+}{\eta_+ - \eta_-}\right] e^{-\lambda_- t} \qquad [2a]$$

$$m_{Ni}(t) = \eta_+ \left[\frac{1 - \eta_-}{\eta_+ - \eta_-}\right] e^{-\lambda_+ t} - \eta_- \left[\frac{1 - \eta_+}{\eta_+ - \eta_-}\right] e^{-\lambda_- t} \qquad [2b]$$

where

$$\eta_\pm = \left(\frac{\tau_{Ex}}{2\tilde{t}}\right)\left[1 \mp \sqrt{1 + \left(\frac{2\tilde{t}}{\tau_{Ex}}\right)^2}\right] \qquad [3a]$$

$$\lambda_\pm = \left(\frac{1}{2\bar{t}} + \frac{1}{\tau_{Ex}}\right) \pm \frac{1}{2\tilde{t}}\sqrt{1 + \left(\frac{2\tilde{t}}{\tau_{Ex}}\right)^2} \qquad [3b]$$

and

$$\bar{t} = \frac{\tau_{Ni}\tau_{Fe}}{\tau_{Ni} + \tau_{Fe}}, \qquad \tilde{t} = \frac{\tau_{Ni}\tau_{Fe}}{\tau_{Ni} - \tau_{Fe}} \qquad [4]$$

Fitting our permalloy-Cu data to this model reproduces the distinct demagnetization dynamics of Fe and Ni on timescales shorter than the exchange time τ_{Ex}, and also the observed delay of Ni with respect to Fe at times larger than τ_{Ex}. It additionally yields a smaller intrinsic demagnetization constant (i.e., the "virtual" constant in the absence of Fe–Ni interatomic exchange coupling) for Fe in comparison to Ni; i.e., $\tau_{Ni} > \tau_{Fe}$, qualitatively consistent with our observations for elemental Fe and Ni (see Fig. 3). For permalloy-Cu, a reasonable fit requires $\tau_{Ni} > 500$ fs, an indication that the Ni itself is barely affected by the pump pulse (see *Supporting Information*, where as expected, the demagnetization times are somewhat different in the alloy and the pure material). The fit to our model thus uncovers a picture validated by measure-

ments: *after a characteristic exchange time τ_{Ex}, the Ni magnetization is essentially "dragged down" by the strong Fe–Ni exchange coupling to the rapidly demagnetizing Fe moments. At this point both moments decay at the same effective time scale $\tau_{Eff} \sim 2\tau_{Fe}$.* We note that the Ni magnetization, when alloyed with Fe, is only weakly affected by the pump pulse immediately after excitation—leading to the very large intrinsic demagnetization constants of τ_{Ni} when the data are fitted to the model. For the case of permalloy with stronger interatomic Fe–Ni exchange coupling, a smaller exchange time τ_{Ex} is expected. Indeed, using the same rate equations, we can reproduce the demagnetization dynamics of permalloy, which is not possible with the usual double exponential decay function. Fitting all our data yields mean values of $\tau_{Ex} = 18 \pm 10$ fs for permalloy, and 76 ± 9 fs for permalloy-Cu (see *Supporting Information*).

Additional support for our interpretation can be found by considering the Landau–Lifshitz equation for magnetization dynamics, where spin relaxation in ferromagnets proceeds at a rate proportional to the gyromagnetic precession frequency. In the present case of disproportionate demagnetization between the Ni and Fe components, we expect local gyromagnetic dynamics to be dominated by interatomic exchange coupling. Based on the values of T_c, the average exchange energy for permalloy-Cu is approximately 3.3 times less than that of pure permalloy (see *Supporting Information*). The ratio of τ_{Ex} extracted from our data for permalloy-Cu relative to permalloy is 4.2 ± 2.8 (corresponding to characteristic exchange times of $\tau_{Ex} = 18 \pm 10$ fs and 76 ± 9 fs, respectively). Thus, the scaling of exchange energy and τ_{Ex} between permalloy and permalloy-Cu are comparable, supporting our interpretation.

The significantly higher intrinsic demagnetization times extracted for Ni, $\tau_{Ni} > 500$ fs, compared to Fe, ($\tau_{Fe} \approx 89 \pm 8$ fs in permalloy and $\tau_{Fe} \approx 126 \pm 9$ fs in permalloy-Cu) indicate that the uniformity of the Ni spins in the alloy are most strongly influenced by the exchange coupling to the Fe, and much less influenced by the laser excitation in comparison to the pure material ($\tau_{Ni,elemental} \approx 157$ fs). In contrast, our data indicate that the laser excitation induces demagnetization for Fe on a comparable timescale to that for an elementally pure material ($\tau_{Fe,pure} \approx 98 \pm 26$ fs). Because of interatomic Fe–Ni exchange coupling, the Ni spins eventually demagnetize with the same time-constant as Fe in the alloys via the thermodynamic contact to the Fe spin bath—but with an apparent delay that is given by τ_{Ex}. Our data indicate that this delay is larger in permalloy-Cu than in permalloy due to the reduced exchange energy. To our knowledge, such a delayed behavior of magnetization dynamics in metallic alloys has not been previously predicted or observed.

Current macroscopic and microscopic models that explain demagnetization dynamics for pure materials need to be extended to alloyed magnetic materials. The absence of such microscopic models for multicomponent systems prevents us from addressing why Ni intrinsically reacts slower in the specific alloys in comparison to the pure Ni material. However, our experiment provides a clear observation of how the strength of the exchange coupling between the constitutive atomic components can influence magnetization dynamics in alloys on ultrafast timescales. As such, our data help elucidate the microscopic role of the fundamental quantum mechanical exchange interaction in the ultrafast demagnetization process.

In summary, we explore the consequences of the fundamental quantum exchange interaction in strongly coupled ferromagnetic systems, showing that quantitatively different magnetization dynamics of the individual elements can be observed on timescales shorter than the characteristic exchange timescale. On longer timescales, the dynamics are dominated by the faster of the two species. Analysis of our data indicates that the observed differences in demagnetization rate are primarily determined by intrinsic properties of the material rather than the result of photo-induced ultrafast transient changes in the material, e.g., hot-elec-

tron-gas screening or nonequilibrium phases. This fact has significant impact for fundamental models of ultrafast magnetism, and for the dynamical magnetic behavior for all types of exchange-coupled materials, including both the alloys and multilayer structures that are widely used for data storage.

Materials and Methods

Experimental Setup. We generate coherent high-harmonics (HHG) by focusing 25 fs laser pulses (780 nm central wavelength) into a neon-filled hollow waveguide. The laser operates at 2 kHz repetition rate with the pulse energy of approximately 2.2 mJ/pulse. Ninety percent of the laser power is used for HHG, while the remaining light is used to excite the sample. The waveguide is filled with neon gas that is pressure tuned to approximately 400 torr in order to phase-match a broad range of harmonics in the range of extreme ultraviolet (XUV) from 35 to 70 eV (21st–43rd harmonic), covering the region of the spectrum where the M-edge resonances of 3d ferromagnetic metals are located. A 200 nm thick Al filter blocks the fundamental laser light. The Al filter limits our highest energy HHG photons to 72 eV as a result of strong absorption above the Al $L_{2,3}$ edges. The HHG beam is refocused onto the grating sample using a grazing incident toroidal mirror. The HHG spot size on the sample is less than 500 µm, which is smaller than the pump laser spot size of approximately 1–2 mm to ensure good spatial overlap and uniform demagnetization. Water-cooling stabilizes the sample temperature at 293 K.

Sample Fabrication. A 10 nm thick permalloy-Cu (($Ni_{0.8}Fe_{0.2})_{0.6}Cu_{0.4}$) alloy thin film was grown by cosputter deposition with permalloy ($Ni_{0.8}Fe_{0.2}$) and pure Cu targets. The rates from a permalloy target and a pure Cu target were calibrated using a quartz crystal monitor and a profilometer. A thin 3 nm Ta seed layer was first sputter deposited onto a thermally oxidized Si(100) wafer to provide a strong (111)-texture and good adhesion prior to depositing the permalloy-Cu alloy. Diffraction gratings were patterned from the film via optical lithography and a subsequent Ar ion milling at 300 eV. The grating consisted of an array of 1 µm wide stripes with a center-to-center spacing of 2 µm. The 10 nm thick permalloy ($Ni_{0.8}Fe_{0.2}$) diffraction grating was fabricated by a direct liftoff process from a film grown by ion beam deposition with a target made from the same source material that was used for sputtering of the permalloy-Cu film. A 3 nm Ta seed layer was also used for adhesion to promote strong (111)-texture prior to depositing the permalloy layer. X-ray diffraction data, magnetometry measurements, ferromagnetic resonance measurements, and static element-specific magnetization measurements presented in the SI verify a random placement of the Fe, Ni, and Cu atoms in single fcc-phase crystal lattice.

1. Pan L, Bogy DB (2009) Heat-assisted magnetic recording. *Nature Photon* 3:189–190.
2. White R, New R, Pease R (1997) Patterned media: A viable route to 50 Gbit/in(2) and up for magnetic recording? *Ieee T Magn* 33:990–995.
3. Stanciu CD, et al. (2007) All-optical magnetic recording with circularly polarized light. *Phys Rev Lett* 99:047601.
4. Nagasaka K (2009) CPP-GMR technology for magnetic read heads of future high-density recording systems. *J Magn Magn Mater* 321:508–511.
5. Schoenlein R, et al. (2000) Generation of femtosecond pulses of synchrotron radiation. *Science* 287:2237–2240.
6. Zholents A, Zolotorev M (1996) Femtosecond X-ray pulses of synchrotron radiation. *Phys Rev Lett* 76:912–915.
7. Stamm C, et al. (2007) Femtosecond modification of electron localization and transfer of angular momentum in nickel. *Nature Mat* 6:740–743.
8. Boeglin C, et al. (2010) Distinguishing the ultrafast dynamics of spin and orbital moments in solids. *Nature* 465:458–U478.
9. Radu I, et al. (2011) Transient ferromagnetic-like state mediating ultrafast reversal of antiferromagnetically coupled spins. *Nature* 472:205–208.
10. Kapteyn H, Murnane M, Christov I (2005) Extreme nonlinear optics: A coherent X rays from lasers. *Phys Today* 58:39–44.
11. Popmintchev T, Chen M-C, Arpin P, Murnane MM, Kapteyn HC (2010) The attosecond nonlinear optics of bright coherent X-ray generation. *Nature Photon* 4:822–832.
12. La-O-Vorakiat C, et al. (2009) Ultrafast demagnetization dynamics at the M edges of magnetic elements observed using a tabletop high-harmonic soft X-ray source. *Phys Rev Lett* 103:257402.
13. Grychtol P, et al. (2010) Resonant magnetic reflectivity in the extreme ultraviolet spectral range: Interlayer-coupled Co/Si/Ni/Fe multilayer system. *Phys Rev B* 82:054433.
14. La-O-Vorakiat C, et al. (2012) Demagnetization measurements using extreme ultraviolet light: Comparison of electronic and magnetic contributions. *Phys Rev X* 2:011005.
15. Bigot J-Y (2012) Spin-sensitive optics. *Physics* 5:11.
16. Radu I, et al. (2009) Laser-induced magnetization dynamics of lanthanide-doped permalloy thin films. *Phys Rev Lett* 102:117201.
17. Carpene E, et al. (2008) Dynamics of electron-magnon interaction and ultrafast demagnetization in thin iron films. *Phys Rev B* 78:174422.
18. Koopmans B, et al. (2010) Explaining the paradoxical diversity of ultrafast laser-induced demagnetization. *Nature Mat* 9:259–265.
19. Bozorth RM (1993) *Ferromagnetism* (IEEE Press, Piscataway, NJ) p 161.

20. Raghavan V (2004) Cu-Fe-Ni (copper-iron-nickel). *J Phase Equilib Diff* 25:547–549.
21. Callen H (1963) Green function theory of ferromagnetism. *Phys Rev* 130:890.
22. Collins M, Minkiewi V, Nathans R, Passell L, Shirane G (1969) Critical and spin-wave scattering of neutrons from iron. *Phys Rev* 179:417.
23. Bigot J-Y, Vomir M, Beaurepaire E (2009) Coherent ultrafast magnetism induced by femtosecond laser pulses. *Nat Phys* 5:515–520.
24. Koopmans B, Ruigrok J, Dalla Longa F, de Jonge W (2005) Unifying ultrafast magnetization dynamics. *Phys Rev Lett* 95:267207.
25. Beaurepaire E, Merle J, Daunois A, Bigot J (1996) Ultrafast spin dynamics in ferromagnetic nickel. *Phys Rev Lett* 76:4250.
26. Zhang GP, Hübner W, Lefkidis G, Bai YH, George TF (2009) Paradigm of the time-resolved magneto-optical Kerr effect for femtosecond magnetism. *Nat Phys* 5:499–502.
27. Krauss M, et al. (2009) Ultrafast demagnetization of ferromagnetic transition metals: The role of the Coulomb interaction. *Phys Rev B* 80.
28. Zhang GP, Hübner W (2000) Laser-induced ultrafast demagnetization in ferromagnetic metals. *Phys Rev Lett* 85:3025–3028.
29. Cinchetti M, et al. (2006) Spin-flip processes and ultrafast magnetization dynamics in Co: Unifying the microscopic and macroscopic view of femtosecond magnetism. *Phys Rev Lett* 97:177201.
30. Djordjevic M, Munzenberg M (2007) Connecting the timescales in picosecond remagnetization experiments. *Phys Rev B* 75:012404.
31. Kazantseva N, et al. (2008) Towards multiscale modeling of magnetic materials: Simulations of FePt. *Phys Rev B* 77:184428.
32. Carva K, Battiato M, Oppeneer P (2011) Is the controversy over femtosecond magneto-optics really solved? *Nat Phys* 7:665.
33. Battiato M, Carva K, Oppeneer PM (2010) Superdiffusive spin transport as a mechanism of ultrafast demagnetization. *Phys Rev Lett* 105:027203.
34. Rohwer T, et al. (2011) Collapse of long-range charge order tracked by time-resolved photoemission at high momenta. *Nature* 471:490.
35. Huber R, et al. (2001) How many-particle interactions develop after ultrafast excitation of an electron-hole plasma. *Nature* 414:286–289.
36. Rhie H, Dürr H, Eberhardt W (2003) Femtosecond electron and spin dynamics in Ni/W(110) films. *Phys Rev Lett* 90:247201.
37. Hübner W, Zhang G (1998) Ultrafast spin dynamics in nickel. *Phys Rev B* 58: R5920–R5923.

Supporting Information

Mathias et al. 10.1073/pnas.1201371109

SI Text

SI Materials and Methods

A) Sample characterization. We would like to present measurements to disprove any possible phase segregation in the alloys used in the experiment, which would lead to distinct differences in magnetization dynamics between Fe and Ni. The results presented below clearly show that phase segregation is not present in our samples.

The sample used for the measurement of elemental Fe and Ni were similar to the grating structures used for alloys, except that the grating consisted of alternating stripes of pure Fe and pure Ni. In this case, 1 μm stripes of Ni with a 4 μm center-to-center spacing were first fabricated by a direct liftoff process. A second lithography step was used to pattern and liftoff 1 μm wide Fe stripes in-between the previously fabricated Ni stripes, yielding alternating stripes of Fe and Ni with a center-to-center spacing of 2 μm. In both cases, the thickness of the individual Ni and Fe layers was 10 nm and a 2 nm Ta seed layer was initially deposited for adhesion. The Fe stripes are capped with a Ta layer (2.5 nm) to prevent oxidation. After removal from the deposition chamber, these samples were quickly transferred to a vacuum storage chamber to minimize oxidation of the surface.

A.1. X-ray diffraction. X-ray diffraction (XRD) measurements were performed using a parallel beam configuration where a Cu K_α source was conditioned with a wavelength-specific X-ray mirror. The diffracted beam optics consisted of a parallel plate collimator, Soller slit, and graphite monochromator prior to detection by a proportional counter. The sample was mounted on a 4-circle goniometer with an instrumental resolution of 0.0001° in 2θ and ω. After a direct-beam alignment of $2\theta = 0$", the sample height was adjusted until it cut the beam in half. The sample tilt angles were then rocked and iterated with the sample height position to ensure that the sample was centered with the surface parallel with respect to the incident X-ray beam.

Fig. S1 shows 2θ- ω scans for the permalloy and permalloy-Cu thin films as well as the permalloy-Cu grating sample used in the experiment. Both the (111) and (222) peaks are present in all the spectra, consistent with a well (111)-textured face centered cubic (fcc) structure. Rocking curves peak widths of $\approx$3–4° at FWHM on the (111) peaks further indicate the high quality of (111)-texture. No additional peaks corresponding to additional phases or segregation of species are present. The measured values of the lattice parameters are 0.3547 nm, 0.3573 nm, and 0.3572 nm for the permalloy thin film, permalloy-Cu thin film, and permalloy-Cu grating, respectively. Furthermore, if a linear relationship of the lattice constant is assumed, then the ideal lattice constant of a solid solution of 60% permalloy and 40% Cu is calculated to be 0.3574 nm (using the measured lattice constant for permalloy above and the bulk value of 0.3615 nm for Cu). The good agreement between the measured and calculated lattice parameters, combined with the lack of any additional peaks in the XRD spectra, confirm that the sample consists of a single fcc phase, solid solution of Ni, Fe, and Cu, as expected for this system.

A.2. SQUID magnetometry. Magnetometry measurements were performed using a superconducting quantum interference device (SQUID) magnetometer. The saturation magnetization was measured as function of temperature from 10 K to 400 K, from which T_C was determined for the permalloy-Cu alloy via extrapolation from the power law dependence of M on T (Fig. S2A). T_C is identical for Fe and Ni, as expected. In addition, we measure a smooth and continuous change of T_C as a function of Cu doping for a full series of samples where the Cu content was varied from 60% to 40% (Fig. S2B). This trend further confirms that our samples consist of a complete intermixture of Fe, Ni, and Cu, without segregation.

A.3. Ratio of exchange energies permalloy/permalloy-Cu. Based on the SQUID data for 60:40 permalloy-Cu, the ratio of the Curie temperature for permalloy/permalloy-Cu is 2.1. The ratio of the exchange energy is therefore 2.1:1 at 0 K. At room-temperature, we need to account for the renormalization of exchange, which scales in proportion to $M(T)/M(T = 0)$. The ratio of this quantity is 1.56, according to the SQUID data. Therewith, the ratio of exchange energies between permalloy and permalloy-Cu at 300 K is about $1.56 \times 2.1 = 3.3$.

A.4. Ferromagnetic Resonance (FMR). We measured the ferromagnetic resonance (FMR) of the permalloy-Cu grating sample with a broadband FMR spectrometer in a perpendicular applied field (P-FMR) geometry. Such measurements provide accurate determination of magnetic homogeneity in the material and the intrinsic damping parameter, α. Details of the experimental technique can be found in Refs. (1–3). The real and the imaginary parts of the magnetic contribution to the transmission parameter S_{21} are fit simultaneously to the complex susceptibility $\chi(H)$.

Fig. S3 shows the FMR data taken on the permalloy-Cu grating sample. Most importantly, we observe a single FMR peak, as expected for an alloy without segregation. Furthermore, we fit the measured resonant fields (blue circles) with the Kittel equation (red line), as shown in Fig. S3.

The Kittel equation in this perpendicular geometry is

$$H_0(f) = \frac{2\pi f}{|\gamma|\mu_0} + M_{\text{eff}},$$

where M_{eff} is the effective magnetization, $\gamma = g\mu_B/h$ is the gyromagnetic ratio, μ_0 is the permeability of free space, f is the applied microwave frequency, μ_B is the Bohr magneton, and g the spectroscopic splitting factor. The fit to the data yields $\mu_0 M_{\text{eff}} = 0.293 \pm 0.001$ T and $g = 2.026 \pm 0.004$. The value for $\mu_0 M_{\text{eff}}$ is lower than the value for the saturation magnetization $\mu_0 M_s$ obtained by SQUID magnetometry. This is likely due to edge effects for a finite width grating structure and anisotropy, which will lower $\mu_0 M_{\text{eff}}$ compared with $\mu_0 M_s$. The measured line width $\Delta H(f)$ (yellow diamonds) is fit with the phenomenological equation (green line) (4):

$$\Delta H(f) = \Delta H_0 + \frac{4\pi\alpha}{|\gamma|\mu_0}f$$

where ΔH_0 is the inhomogenous line width broadening, generally attributed to locally varying magnetic properties of the sample. The linear fit yields $\mu_0 \Delta H_0 = 5.6 \pm 0.2$ mT and $\alpha = 0.0158 \pm 0.0002$. Both of these values are elevated compared to permalloy films without alloying Cu. The value of α is higher than that of 0.005 for pure $Ni_{0.8}Fe_{0.2}$ (5), which is expected since T_C of the permalloy-Cu sample is relatively close to room temperature (6). The inhomogeneity of the perpendicular anisotropy $\mu_0 \Delta H_0 = 5.6 \pm 0.2$ mT is indicative of a high quality thin film with relatively small variation of magnetic properties within the material.

A.5. Static T-MOKE asymmetry measured by HHG. We also measured the static asymmetry parameter for permalloy-Cu as a function of sample temperature up to 425 K, which exceeds the Curie-temperature. Fig. S4 shows the measurement results. The Fe and Ni M-edge asymmetry signals have the same temperature dependence and both asymmetries gradually reduce to zero near the Curie temperature. The power law fit gives the Curie temperature of 407.5 ± 3.7 K for Ni and 403.5 ± 1.1 K with critical exponent β of little less than 0.5—the value from mean-field theory. The fact that both the Fe and Ni signals show the same Tc to within error bars (and not 1043 K and 631 K as expected for bulk Fe and Ni, respectively) implies that we have a single-phase alloy without any segregation between the Fe and Ni. The value of Curie temperature is 5% less than the value measured by SQUID method (Fig. S2) due to expected variations in the sputter deposition rate from different sample to sample.

B) Experimental methods.
B.1. T-MOKE asymmetry. By matching the electromagnetic boundary conditions at the interface, the reflection coefficient in T-MOKE geometry for p- and s-polarized light can be written as (7, 8)

$$r_{pp}^{\pm} = \frac{n \cos \theta_i - n_0 \cos \theta_t}{n \cos \theta_i + n_0 \cos \theta_t} \pm \frac{2 i n_0^2 \sin \theta_i \cos \theta_i}{(n \cos \theta_i + n_0 \cos \theta_t)^2} Q$$

$$r_{ss} = \frac{n_0 \cos \theta_i - n \cos \theta_t}{n_0 \cos \theta_i + n \cos \theta_t},$$

where n_0 and n are refractive indices of the incident nonmagnetic medium (vacuum, in our case) and the reflecting magnetic sample, respectively. θ_t is the refracted angle and θ_i is the angle of incidence onto the magnetized sample. The first terms in each equation are from the optical response (Fresnel coefficients) while the Voigt parameter Q describes the magneto-optic effect, which is related to the magnetization vector through the off-diagonal element of the dielectric tensor. Only the p-polarized reflection depends on the magnetization (9). The sign of r_{pp} depends on the orientation of the magnetization aligned by the external magnetic field. Finally, the asymmetry parameter A described in the text is related to the r_{pp} coefficient as:

$$A = \frac{I_+ - I_-}{I_+ - I_-} = \frac{|r_{pp}^+|^2 - |r_{pp}^-|^2}{|r_{pp}^+|^2 + |r_{pp}^-|^2}$$

The shape of the T-MOKE asymmetry near an absorption edge is understood (9–14). The function depends sensitively on θ_i, the photon energies through n, and Q. The asymmetry A is usually maximized near an absorption edge. We operated at an angle of incidence near the Brewster's angle of $\theta_i \approx 45°$ to maximize A.

B.2. Time zero determination. The absolute time zero of the dynamics is determined experimentally via autocorrelation with a BBO crystal positioned between the pump laser and the fundamental laser beam, where the second harmonic propagates collinearly with the high-harmonics. The accuracy is within ± 10 fs. Finally, the zero delays for Fe and Ni signals reported in the main text are identical since we record all data in parallel.

B.3. Photon energy calibration. To calibrate the photon energy E of the high-order harmonics, we use the diffraction formula for gratings generalized for any angle of incidence α and diffracted angle β (15)

$$d(\sin \alpha - \sin \beta) = m\lambda,$$

where d is the grating period (2 µm for permalloy and permalloy-Cu, 4 µm for Fe-Ni stripes), m is the diffraction order and λ is the

wavelength. The photon energies of the harmonics are odd multiples (N) of the fundamental energy ($E = \frac{hc}{\lambda} = NE_0$), and the angle of incidence is $\alpha = 45°$.

From geometry, the diffracted angle β can be related to the angle of incidence α, sample-to-CCD distance z, and the diffracted distance along the CCD x by the following relation

$$\beta = \alpha \mp \frac{x}{z},$$

where the minus (plus) sign is used in the case of positive (negative) diffraction orders.

After expanding the diffracted formula around $\alpha = 45°$, the equation reduces to

$$\frac{x}{z} = \sqrt{2} \frac{mhc}{NE_0 d}$$

This equation allows us to relate the measurable distance x to the known order of harmonics N by performing a fit between the two parameters and setting E_0 as a fitting parameter.

C) Data Analysis.
C.1. Influence of sample grating structure and different photon attenuation lengths. In the main text, we extract the time-resolved data at the locations of the high harmonics that give the largest T-MOKE asymmetry and have the highest photon flux. We averaged over 25 time-resolved traces to get sufficient signal-to-noise ratios for the fitting functions. The best signal of Ni (Fe) can be extracted from the harmonics at 67 eV (54 eV) for the permalloy sample.

The high harmonic at 67 eV (Ni) had sufficient intensity to give good signal/noise in the first *and* second order diffraction pattern, see Fig. S5A, *Inset* (blue and green bar, respectively). When we extract the demagnetization dynamics from both orders, we find very good agreement of our fitting results (See Fig. S5A). This measurement confirms that the grating structure of the sample does not artificially contribute spurious signal to our time-resolved measurements.

Different attenuation lengths of the pump pulse and the harmonics used to extract the demagnetization dynamics at the Fe and Ni M-edges yield a different probing depth of the sample, with different effective fluences (excitation densities) probed. However, for a sample thickness of 10 nm and attenuation lengths varying between about 9 nm and 15 nm in permalloy and permalloy-Cu in the relevant XUV range [from The Center for X-ray Optics, http://www.cxro.lbl.gov] (see Fig. S5B), effective fluence differences are in the 1–2% range. For example, the largest attenuation length is found for photons just below the Fe absorption edge in permalloy and is about 15 nm. Using Beer-Lambert law, the sample depth at which the mean of the Beer-Lambert function for a sample thickness of 10 nm and photons travelling in and out of the sample is found is 4.45 nm from the surface. With an attenuation length of 17 nm for the infrared pump pulse (16), this corresponds to an effectively measured fluence of 77% of the total impinging fluence. On the other hand, the lowest attenuation length is found for photons with energies just above the Ni edge and is about 9.1 nm, yielding a mean of the Beer-Lambert exponential decay function at 4.12 nm sample depth. This corresponds to a fluence of 78.5% of the total fluence. As can be seen from Ref. (17) of the main text, fluence differences in the 1–2% region influence the exponential decay constant only on a sub-2 fs timescale for Ni (where typical demagnetization times in the alloys are ≈ 160 fs). Please note, however, that such probing-depth-induced fluence-dependence can affect the demagnetization constants, but cannot produce the observed delayed behavior as discussed in the paper.

In the case of elemental Fe and Ni, the attenuation lengths in the XUV vary between 6 and 25 nm, see Fig. S5B. The attenuation lengths of the pump pulse for elemental Fe and Ni also need to be considered and are in the region of 35 nm and 24 nm, respectively, calculated using Fresnel equations and refractive indexes (17). The same calculation with Beer-Lambert exponential decay function for the according attenuation lengths in Fe and Ni yields effective fluence differences in the 2–4% region, so that the difference of the exponential demagnetization decay constant is on a sub-5 fs timescale.

Finally, the different harmonics take the same physical path in the beamline, using grazing-incidence reflective optics, and a thin filter to reject the laser light. The relative delay through such filters have been measured in the attosecond range (18). Thus, the harmonics all arrive at the sample at the same time (well within our error bars).

C.2. Fitting results

When we fit our data to the rate-equation model (Eq. 2), and we allow all parameters to vary, the intrinsic demagnetization time for Ni τ_{Ni} diverges [the intrinsic demagnetization times are the artificial time constants for Fe and Ni given by the rate-equation model, which describes Fe and Ni being (i) alloyed to permalloy and (ii) in the absence of exchange coupling]. This indicates that the Ni spins are only weakly influenced by the pump pulse such that we are insensitive to the value of τ_{Ni} in the context of fitting the data with Eq. 2. To determine a reasonable lower bound for τ_{Ni}, we investigated the fractional uncertainty in the exchange time τ_{Ex} using fixed values of τ_{Ni}. This procedure establishes a reasonable lower bound for τ_{Ni}. Using the criterion that the fractional error in τ_{Ex} does not exceed twice the minimum possible, we find $\tau_{Ni} > 504$ fs for permalloy-Cu. If τ_{Ni} is constrained to be smaller than this amount, the error for τ_{Ex} is unacceptably large. The fitting results presented in the manuscript are extracted when all parameters are allowed to vary.

Fluence-dependent data of the ultrafast demagnetization in permalloy-Cu yield identical dynamics to within our error bars. In particular, we do not see any fluence dependence in the demagnetization delay between Fe and Ni, which we would have expected if highly excited hot electrons were responsible for the observed dynamics. Fig. S6 shows the data for pump fluences of 300 mW ($q = 0.6$) and 250 mW ($q = 0.5$) with the fit to the model (with q the maximum quenching of the magnetization $q = A_{min}/A_0$). [Data for pump fluence of 360 mW ($q = 0.77$) is shown in the main paper]. The fluence-dependent data has been collected in the same measurement period in order to achieve maximum comparability. All fitting results are summarized in Tables S1 and S2. The mean values for the exchange times τ_{Ex} are 18 ± 10 fs for permalloy and 76 ± 9 fs for permalloy-Cu.

We note once again that the Ni magnetization, when alloyed with Fe, is only weakly affected by the pump pulse immediately after excitation—leading to the very large intrinsic demagnetization constants of τ_{Ni} when the data are fitted to the model.

The elemental data for Fe and Ni was fitted using a simple double exponential fitting function given by $m(t) = 1 - \Delta m[1 - \exp(-t/\tau_m)]\exp(-t/\tau_r)$. The fitting results are, as given in the paper, $\tau_m = 98 \pm 26$ fs for elemental Fe and 157 ± 9 fs for elemental Ni (with recovery time constants $\tau_r = 11 \pm 7$ ps for Fe, and $\tau_r = 9 \pm 1$ ps for Ni, respectively). Here, we note that one usually compares demagnetization constants for identical quenching parameters q, in which case one would expect the opposite behavior to a first approximation: Ni should demagnetize faster than Fe due to the much lower Curie temperature of Ni (19). Here, however, the measurement is carried out in a parallel detection scheme with *identical* laser fluence, so that the magnetization quenching q of Fe is considerably lower than that of Ni (19% vs. 45%, respectively, see Fig. 3A in main text). As a consequence, the demagnetization constant for Fe is smaller than the demagnetization constant for Ni under these excitation conditions.

1. Kalarickal S, et al. (2006) Ferromagnetic resonance linewidth in metallic thin films: Comparison of measurement methods. *J Appl Phys* 99:093909
2. Nembach HT, et al. (2011) Perpendicular ferromagnetic resonance measurements of damping and Lande g- factor in sputtered (Co2Mn)(1-x)Ge-x thin films. *Phys Rev B* 84:054424
3. Neudecker I, et al. (2006) Comparison of frequency, field, and time domain ferromagnetic resonance methods. *J Magn Magn Mater* 307:148–156
4. Rossing T (1963) Resonance linewidth and anisotropy variation in thin films. *J Appl Phys* 34:995
5. Shaw JM, Silva TJ, Schneider ML, McMichael RD (2009) Spin dynamics and mode structure in nanomagnet arrays: Effects of size and thickness on linewidth and damping. *Phys Rev B* 79:184404
6. Atxitia U, Chubykalo-Fesenko O, Walowski J, Mann A, Muenzenberg M (2010) Evidence for thermal mechanisms in laser-induced femtosecond spin dynamics. *Phys Rev B* 81:174401
7. Zvezdin AK, Kotov VA, *Modern Magnetooptics and Magnetooptical Materials: Studies in Condensed Matter* (Taylor & Francis Group, Boca Raton, FL, 1997) .
8. Grychtol P, et al. (2010) Resonant magnetic reflectivity in the extreme ultraviolet spectral range: Interlayer-coupled Co/Si/Ni/Fe multilayer system. *Phys Rev B* 82:054433
9. La-O-Vorakiat C, et al. (2009) Ultrafast demagnetization dynamics at the M edges of magnetic elements observed using a tabletop high-harmonic soft X-ray source. *Phys Rev Lett* 103:257402
10. Hillebrecht F, et al. (1995) New magnetic linear dichroism in total photoelectron yield for magnetic domain imaging. *Phys Rev Lett* 75:2224–2227
11. Pretorius M, et al. (1997) Transverse magneto-optical Kerr effect of Fe at the Fe 3p threshold. *Phys Rev B* 55:14133–14135
12. Sacchi M, Panaccione G, Vogel J, Mirone A, van der Laan G (1998) Magnetic dichroism in reflectivity and photoemission using linearly polarized light: 3p core level of Ni(110). *Phys Rev B* 58:3750–3754
13. Hecker M, Oppeneer P, Valencia S, Mertins H, Schneider C (2005) Soft X-ray magnetic reflection spectroscopy at the 3p absorption edges of thin Fe films. *J Electron Spectrosc* 144–147:881–884
14. Hochst H, Rioux D, Zhao D, Huber D (1997) Magnetic linear dichroism effects in reflection spectroscopy: A case study at the Fe M-2,M-3 edge. *J Appl Phys.* 81:7584–7588
15. Hecht E, *Optics* (Addison Wesley, New York, 2001).
16. Giannetti C, et al. (2007) Thermomechanical behavior of surface acoustic waves in ordered arrays of nanodisks studied by near-infrared pump-probe diffraction experiments. *Phys Rev B* 76:125413
17. Johnson P (1974) Optical constants of transition metals: Ti, V, Cr, Mn, Fe, Co, Ni, and Pd. *Phys Rev B* 9:5056
18. Lopez-Martens R, et al. (2005) Amplitude and phase control of attosecond light pulses. *Phys Rev Lett* 94:033001
19. Carpene E, et al. (2008) Dynamics of electron-magnon interaction and ultrafast demagnetization in thin iron films. *Phys Rev B* 78:174422.
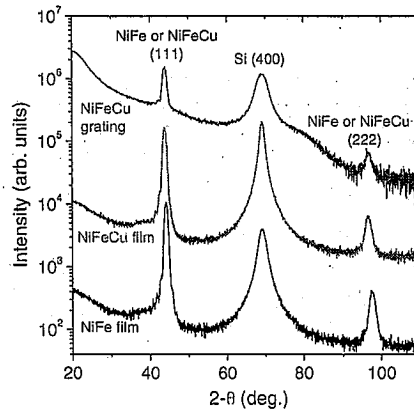
Fig. S1. XRD 2θ- ω scans for the permalloy thin film (NiFe film), permalloy-Cu thin film (NiFeCu film), and permalloy-Cu grating (NiFeCu grating) sample.
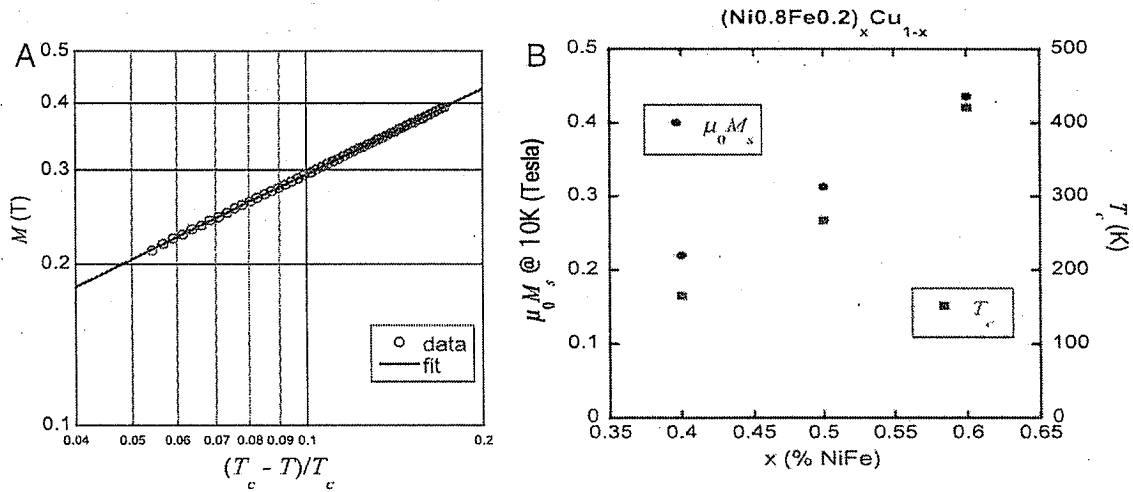

Fig. S2. (*A*) SQUID measurement of permalloy-Cu thin film that shows the saturation magnetization as a function of temperature. The fitted Curie temperature is $T_C = 423$ K and the critical exponent is $\beta = 0.53$. (*B*) Measured Curie temperature (red square dot, right axis) and saturation magnetization (blue circle, left axis) as a function (x) of permalloy (NiFe) content (or 1—x as copper content).
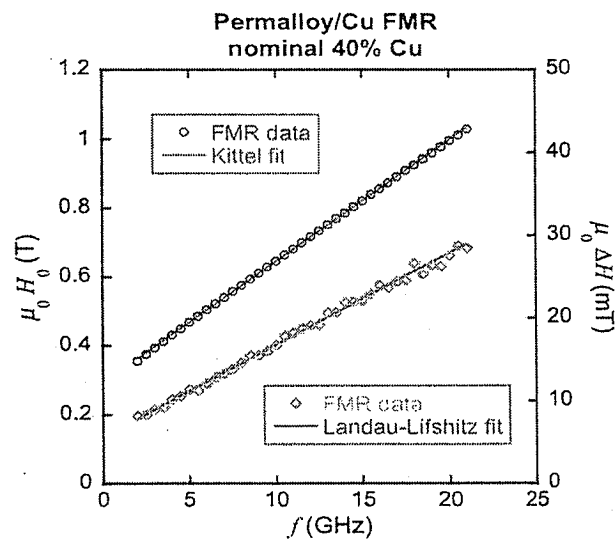
Fig. S3. Ferromagnetic resonance field (blue circles) and line width (orange diamonds) as a function of microwave frequency for the $(Ni_{0.8}Fe_{0.2})_{0.6}Cu_{0.4}$ grating sample. The red and green lines through the data are fits used to determine the magnetic parameters.
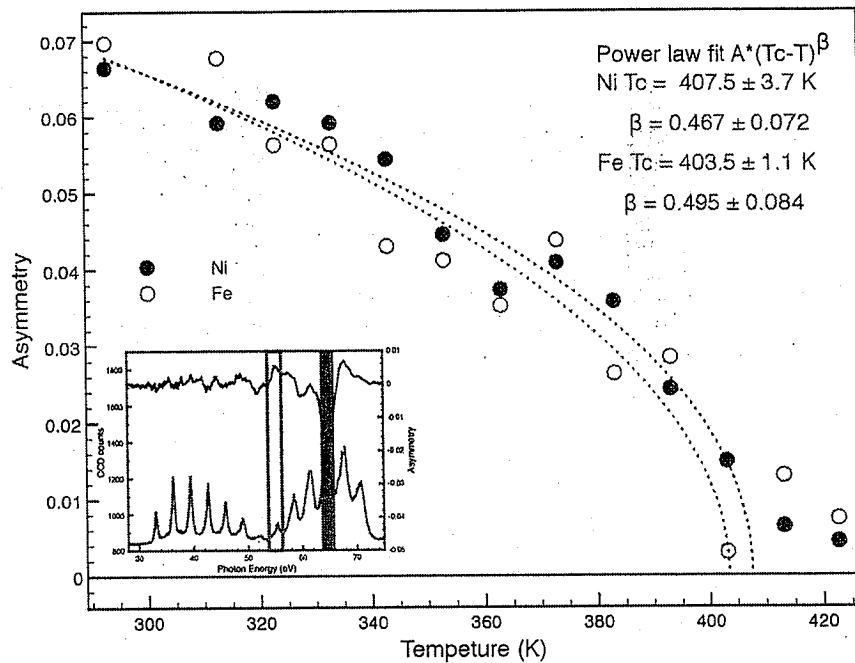
Fig. S4. Static asymmetry parameter of the permalloy-Cu grating sample as a function of temperature. Fe (Ni) *M*-edge signal is shown as red (blue) dots. The HHG spectrum (green) and asymmetry (blue) recorded at room temperature are shown in the inset. The harmonics used to extract the asymmetry around Fe and Ni M-edges are shaded in red and blue, respectively. The sample is magnetized to saturation by a magnetic field of $\approx \pm 40$ Oe.
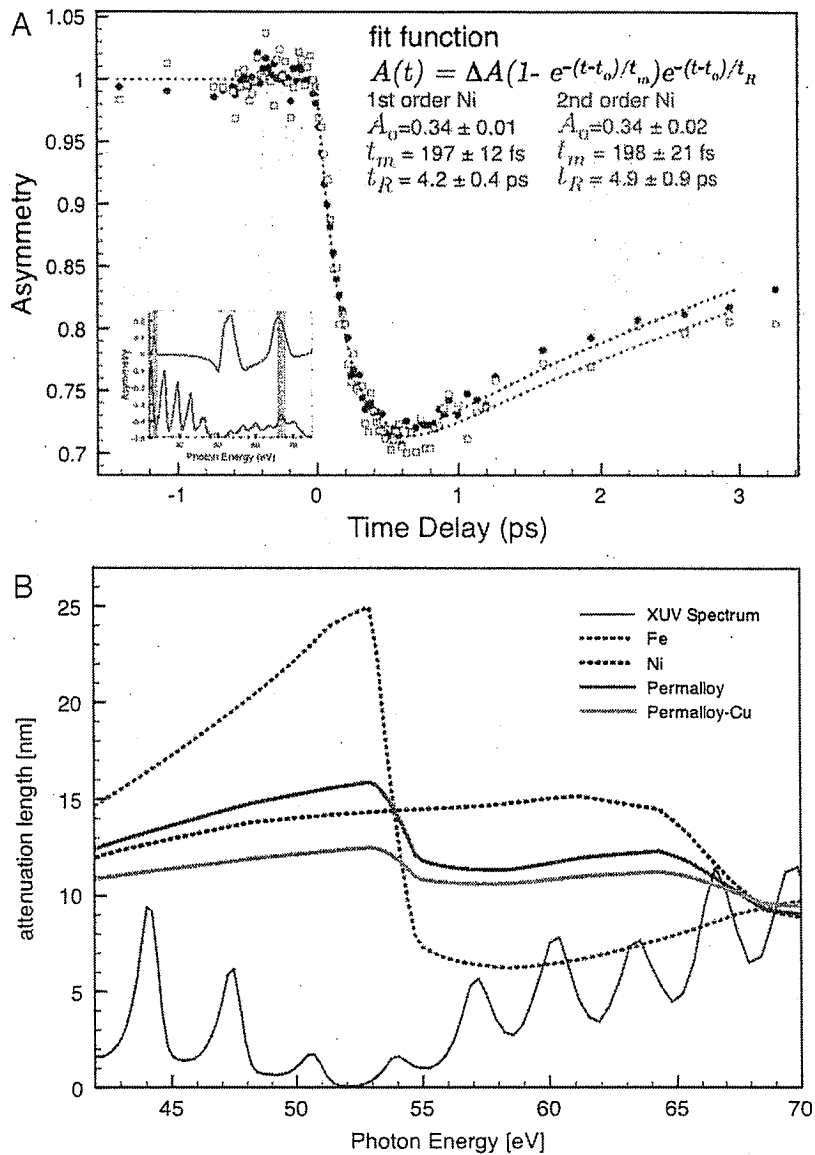
A

fit function

$$A(t) = \Delta A(1 - e^{-(t-t_o)/t_m})e^{-(t-t_o)/t_R}$$

1st order Ni

$A_0 = 0.34 \pm 0.01$
$t_m = 197 \pm 12 \text{ fs}$
$t_R = 4.2 \pm 0.4 \text{ ps}$

2nd order Ni

$A_0 = 0.34 \pm 0.02$
$t_m = 198 \pm 21 \text{ fs}$
$t_R = 4.9 \pm 0.9 \text{ ps}$

Fig. S5. (*A*) Element-selective laser induced demagnetization dynamics of Ni extracted from first (blue) and second order (green) of the 67 eV harmonic in the diffraction pattern. Clearly, the grating does not artificially contribute signal to our time-resolved measurements. (*B*) Attenuation lengths in Fe, Ni, permalloy and permalloy-Cu in the XUV energy region [from The Center for X-ray Optics, http://www.cxro.lbl.gov].
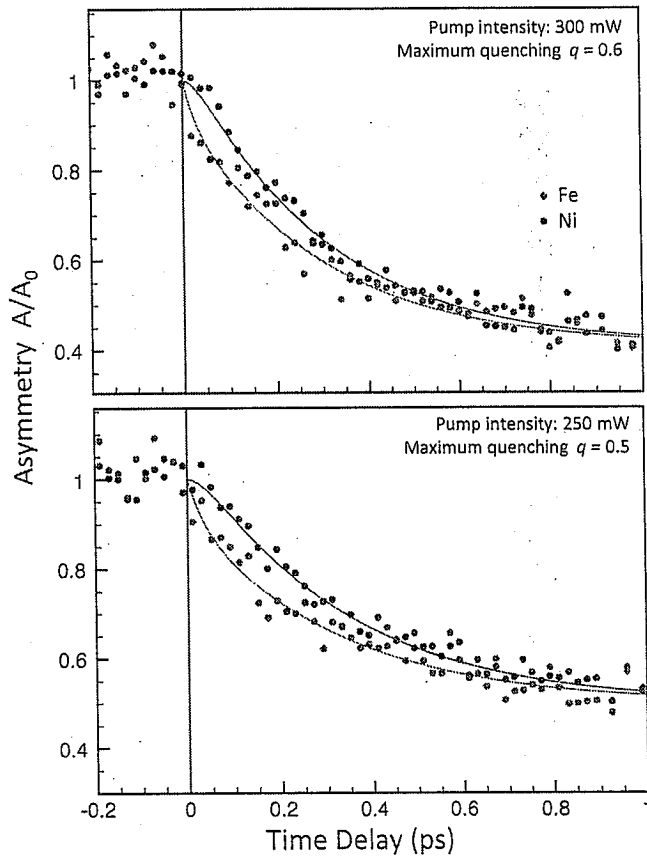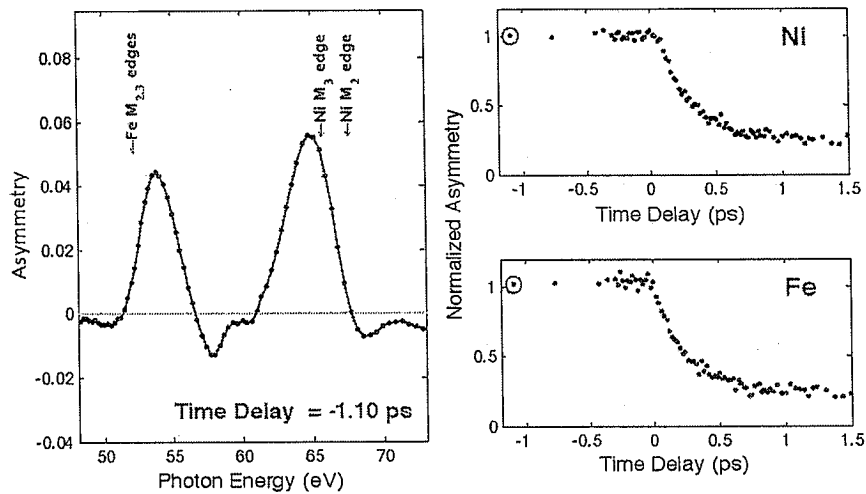
Fig. S6., Pump-fluence dependent data of the permalloy-Cu sample. The data series has been collected in a single experimental measurement period to achieve maximum comparability. The corresponding data for a pump intensity of 360 mW and $q = 0.77$ is shown in the main paper, Fig. 3C.

Movie S1. Element-specific ultrafast demagnetization dynamics of Fe and Ni in permalloy-Cu. Left: Magnetic asymmetry signal of Fe around 54 eV and Ni around 66 eV. The movie shows the evolution of the asymmetry signal as a function time delay between pump and probe pulses, as indicated by "Time Delay" at the bottom of the graph. Right top and bottom: according extracted demagnetization signal for Fe (bottom) and Ni (top). The circles indicate the momentary extracted data points of the magnetization of Fe and Ni, which correspond to the current "Time Delay" in the movie.

Movie S1(M4V)

Table S1. Fitting results for all collected datasets: permalloy

PERMALLOY

q	Δq	τ_{Ex} (fs)	$\Delta\tau_{Ex}$ (fs)	τ_{Fe} (fs)	$\Delta\tau_{Fe}$ (fs)	τ_{Ni} (ps)	$\Delta\tau_{Ni}$ (ps)	τ_{Re} (ps)	$\Delta\tau_{Re}$ (ps)
0.56	0.01	32	11	83	7	5.70×10^{05}	3.1×10^{04}	8.90	0.76
0.35	0.01	14	6	103	5	1.00×10^{05}	3.1×10^{03}	6.45	0.57
0.29	0.01	12	11	93	10	8.02×10^{04}	4.7×10^{03}	5.13	0.07
0.22	0.01	14	10	80	8	6.43×10^{04}	3.7×10^{03}	4.42	0.05
Mean:		18	10	89	8				

q is the maximum quenching of the magnetization; i.e., the minimum asymmetry value reached in the time-resolved experiment normalized by the total asymmetry. τ_{Re} is the exponential time constant for the return of the asymmetry signal to its thermal equilibrium value

Table S2. Fitting results for all collected datasets: permalloy-Cu

PERMALLOY-CU

q	Δq	τ_{Ex} (fs)	$\Delta\tau_{Ex}$ (fs)	τ_{Fe} (fs)	$\Delta\tau_{Fe}$ (fs)	τ_{Ni} (ps)	$\Delta\tau_{Ni}$ (ps)	τ_{Re} (ps)	$\Delta\tau_{Re}$ (ps)
0.82	0.04	67	14	133	16	1.07×10^{08}	4.9×10^{06}	2.28×10^{09}	10^{17}
0.77	0.01	66	6	112	5	1.45×10^{06}	3.2×10^{04}	115	103
0.6	0.01	61	8	132	8	1.86×10^{06}	4.9×10^{04}	43.3	20.8
0.52	0.01	96	8	114	5	7.36×10^{05}	1.9×10^{04}	25.8	4.1
0.50	0.01	88	10	139	11	1.39×10^{05}	4.3×10^{03}	29.3	12.3
Mean:		76	9	126	9				

q is the maximum quenching of the magnetization; i.e., the minimum asymmetry value reached in the time-resolved experiment normalized by the total asymmetry. τ_{Re} is the exponential time constant for the return of the asymmetry signal to its thermal equilibrium value